Effect of strain rate on tensile mechanical properties of high-purity niobium single crystals for SRF applications

Jean-François Croteau, Eureka Pai Kulyadi, Chaitanya Kale, Derek Siu, Di Kang, Ana Teresa Perez Fontenla, Elisa García-Tabarés Valdivieso, Thomas R. Bieler, Philip Eisenlohr, Kiran N. Solanki, et al.

Version of Record: https://www.sciencedirect.com/science/article/pii/S092150932031323X
Manuscript_041a41c20e8ad2c2663c1aef0908357c

Effect of Strain Rate on Tensile Mechanical Properties of High-Purity Niobium Single Crystals for SRF Applications

J.-F. Croteau[a,f*], E. Pai Kulyadi[b], C. Kale[c], D. Siu[d], D. Kang[b], A.T. Perez Fontenla[e], E. García-Tabarés Valdivieso[e], T.R. Bieler[b], P. Eisenlohr[b], K.N. Solanki[c], D. Balint[d], P.A. Hooper[d], S. Atieh[e], N. Jacques[f], E. Cantergiani[a1+]

[a]I-Cube Research, 30 boulevard de Thibaud, 31104, Toulouse, France;

[b]Chemical Engineering and Materials Science, Michigan State University, East Lansing, Michigan 48824-1226, USA;

[c]School for Engineering of Matter, Transport, and Energy, Arizona State University, Tempe, AZ 85287, USA;

[d]Department of Mechanical Engineering, Imperial College London, London, SW7 2AZ, United Kingdom;

[e]European Organization for Nuclear Research (CERN), 1211 Geneva, Switzerland;

[f]ENSTA Bretagne, UMR CNRS 6027, IRDL, 2 rue François Verny, Brest Cedex 9 F-29806, France

[*]jean-francois.croteau@icube-research.com

[+]e.cantergiani@mpie.de

Abstract

An investigation of the mechanical properties of high-purity niobium single crystals is presented. Specimens were cut with different crystallographic orientations from a large grain niobium disk and uniaxial tensile tests were conducted at strain rates between 10^{-4} and 10^{3} s^{-1}. The logarithmic strain rate sensitivity for crystals oriented close to the center of a tensile axis inverse pole figure (IPF) is ~0.14 for all strain rates. The strain at failure (ranging from 0.4 to 0.9) is very sensitive to crystal orientation and maximal at ~10^{-2} s^{-1} for crystals oriented close to the center of an IPF. The high anisotropy observed at quasi-static strain rates decreased with increasing strain rate. The activation of multiple slip systems in the dynamic tests could account for this reduction in anisotropy. A transition from strain hardening to softening in the plastic domain was observed at strain rates greater than approximately $6x10^{-2}$ s^{-1} for crystals oriented close to the center of a tensile axis IPF. Shear bands were observed in specimens with orientations having similarly high Schmid factors on both {110} and {112} slip families, and they are correlated with reduced ductility. Crystal rotations at fracture are compared for the different orientations using scanning electron microscopy images and EBSD orientation maps. A rotation toward the terminal stable [101] orientation was measured for the majority of specimens (with tensile axes more than ~17° from the [001] direction) at strain rates between $1.28x10^{-2}$ and 1000 s^{-1}.

Keywords: stress/strain measurements; niobium; single crystal; high strain rate; anisotropy; SRF

[1] Present address: Max-Planck-Institut für Eisenforschung, Max-Planck-Straße 1, 40237 Düsseldorf, Germany

1 Introduction

1.1 Fabrication of Large Grain SRF Cavities

The fabrication of bulk niobium superconducting radiofrequency (SRF) cavities with improved performance and reduced cost is paramount for enabling future particle accelerators with higher collision energies. The use of large grain niobium, with grains on the order of tens of centimeters instead of polycrystalline niobium blanks with ~50 μm grain size, can reduce the production cost of particle accelerators [1]. Large grain niobium cavities have been fabricated by deep drawing at Jefferson Laboratory [2], [3], Deutsches Elektronen-Synchrotron (DESY) [4], Peking University (PKU) [5], [6], and the Institute of High Energy Physics (IHEP) [7], [8]. Forming of large grain disks with anisotropic mechanical properties results in non-uniform deformation and forming defects such as earing at the equator and iris, but high accelerating gradients were still measured in the SRF cavities [1], [2], [7]. A quantitative understanding of the mechanical properties of niobium single crystals in different orientations is necessary to predict forming.

Moreover, electro-hydraulic forming (EHF) is a novel technique for manufacturing half-cells that has recently gained the attention of the SRF community due to its increased shape accuracy, reduced surface roughness and removal of intermediate annealing steps [9]. Fine-grain niobium 700 MHz half-cells and 400 MHz oxygen-free electronics (OFE) copper half-cells have been successfully formed with this high velocity forming technique [9]. However, manufacturing half-cells from large-grain disks has never been accomplished by EHF or any other high-velocity sheet forming process and the mechanical properties of high-purity niobium single crystals in compression and tension are unknown for strain rates larger than 10^{-1} s^{-1}.

1.2 Mechanical Properties of Niobium Single Crystals

The mechanical properties of niobium single crystals at low strain rates have been investigated since the 1950s, when the element was still called Columbium [10]. Extensive research on the mechanical properties for different orientations, temperatures, and strain rates of high-purity single crystals took place in the 1960s [11]–[16].

Renewed interest in the topic arose at the beginning of the 21st century with the fabrication of SRF cavities with large grain disks. The tensile mechanical properties of niobium single crystals cut from large-grain disks used for the fabrication of SRF cavities have been measured at several universities and research laboratories, but never at strain rates larger than 10^{-1} s^{-1}. The effects of crystal orientation [11], [14], [17]–[20], heat treatment [13], [14], [20]–[23], interstitial hydrogen content [21]–[23], testing temperature [14], [24], [25] and strain rate [11], [14], [22], [23] on mechanical properties of niobium single crystals have been published in literature.

Mitchell et al. [11] performed tensile tests at a nominal strain rate of 4.5×10^{-5} s^{-1} in seven different orientations. No trends were observed for most of the hardening parameters, i.e. the hardening rate of the three stages of single crystal deformation and the shear stress at their beginning and end. The extent of hardening stages I and II were lower for orientations closer to the [001]-[101] symmetry boundary. Specimens on the boundary showed no stage I (easy glide), higher yield stress [14], and

the lowest strain at failure [11]. The [101] orientation is the terminal stable tensile orientation of BCC metals [26].

Duesbery et al. [14] observed slip traces on only {110} and {112} planes in niobium single crystals with differences in the critical resolved shear stress (CRSS) for the two families. Ermakov et al. [17] observed anisotropic tensile properties in the plastic regime with different hardening behaviors and strain at fracture for three different orientations. According to Gnäupel-Herold et al. [22], the differences in yield stress, hardening stages, and the presence or absence of a yield drop cannot be solely attributed to anisotropy but are also probably affected by sample inhomogeneities and purity.

Baars et al. [18] calculated the Schmid factor of the 24 {110} and {112} potential slip system families for large grains within a sliced sheet of a niobium ingot to select the tensile orientations of specimens such that the resolved shear stress on selected slip systems is maximized. Tests were interrupted before failure and lattice orientation gradients were measured to quantify the rotation of the single crystals. A larger misorientation spread within the crystal after deformation was measured for three orientations close to the [001]–[111] and [001]–[101] boundaries of the IPF, and these showed the highest strain hardening. This could be explained by dislocation tangles in cases where the active systems have Burgers vectors in different directions [18]. Finally, it was concluded that the highest resolved shear stress might not lead to the activation of that slip system but that a more complicated criterion involving non-Schmid behavior governs slip [18].

The effect of hydrogen interstitials was studied independently of the heat treatment by Myneni [21] following buffered chemical polishing (BCP) of specimens and by Gnäupel-Herold et al. [22] and Ricker et al. [23] following electrical discharge machining (EDM) of specimens immersed in water. A reduction of yield stress was reported in all studies with increasing hydrogen content. Ricker et al. [23] noted that residual stresses on the surfaces from EDM could affect the mechanical properties and potentially result in greater stresses at that surface compared to the bulk of the specimen. The presence of hydrogen interstitial atoms also leads to a reduction of ductility. This phenomenon, called hydrogen embrittlement, also results in a reduction of ultimate tensile strength and a change in fracture mode that is detrimental for all sheet forming processes [27], [28]. The lack of quantification of the hydrogen (and other impurity) content in published results complicates any attempt for quantitative comparison between different studies.

The effect of strain rate on the tensile properties were reported by Mitchell et al. [11], Duesbery and Foxall [14], Gnäupel-Herold et al. [22], and Ricker et al. [23] for quasi-static strain rate ranges of $4.5\text{x}10^{-6}$ to $1\text{x}10^{-1}$ s^{-1}, $3.4\text{x}10^{-6}$ to $3.4\text{x}10^{-2}$ s^{-1}, and $3\text{x}10^{-6}$ and $4\text{x}10^{-5}$ s^{-1}, respectively. Mitchell et al. and Duesbery and Foxall observed increases in yield stress for increasing strain rates, a common result for BCC metals. Ricker et al. however obtained the opposite trend at nominal strain rates of $4\text{x}10^{-5}$ and $3\text{x}10^{-6}$ s^{-1} [23]. Ricker et al. explained the strain rate effect by the influence of oxygen and hydrogen based upon the work of Ravi and Gibala [29], [30]. At low strain rates and room temperature, the diffusion rate of H is significant enough to produce strain rate effects due to an increased interaction time between the dislocations and the mobile interstitial atoms. At higher strain rates, the dislocations break free and travel unimpeded in the grain. This could also explain

the reduction in failure strain for the case with the smallest strain rate. However, Mitchell et al. performed tests at similar rates but observed an increase in yield stress with increasing strain rate. Since the impurity content in both studies are not reported, no conclusion can be made on the effect of strain rate on the yield stress at such low rates. Mitchell et al. [11] and Duesbery and Foxall [14] also compared the different hardening stages of specimens with a similar crystal tensile orientation. The transition from stage I to II was not well defined at the higher strain rates and a lower stage II hardening rate was measured with increasing strain rates.

From the literature review, it appears that the behavior of niobium single crystals at high strain rate (larger than 10^{-1} s^{-1}) has never been investigated. There is a clear need for this knowledge to enable high-speed forming of large grain Nb into complex shapes such as SRF cavities. The aims of this paper are twofold: (1) to investigate the orientation dependent tensile properties of niobium single crystals in a wide range of strain rates and (2) to provide a database of mechanical properties for high-speed sheet forming of SRF cavities. The effect of the crystallographic orientation and strain rate on the plastic behavior are examined using tensile tests in 18 different orientations and at strain rates from 10^{-4} to 10^{3} s^{-1}. To ensure systematic comparability, all specimens were machined from the same niobium ingot disk.

2 Experimental Procedure

2.1 Niobium Disk Material Fabrication

A 322 mm diameter and 3.8 mm thick high-purity large-grain niobium disk used for the manufacturing of SRF cavities was used. The original ingot purchased by CERN specified a residual resistivity ratio (RRR) greater than 300, implying that the ingot had been electron beam melted multiple times to purify it. The large grains are sections of long columnar grains such that multiple slices have the same orientations and nearly the same grain shapes. More details about the manufacturing of large grain niobium disks and the purification steps are available in a detailed review paper [31]. Single crystalline specimens were cut by electron discharge machining (EDM) from the ten largest grains, with principal dimensions ranging from 45x60 mm^2 to 120x170 mm^2, as illustrated in Figure 1a.

2.2 Orientation Measurement

Measurement of crystallographic orientation of the ten grains from which specimens were cut was performed at Michigan State University using a non-destructive Laue X-ray diffraction method previously developed for this purpose by Kang et al. [32]. The diffraction patterns are measured and indexed to determine the orientation of each grain. Measurements were performed at multiple locations in the largest grains (Figure 1a) to assess whether orientation gradients were present, see Figure 1b. Additional measurements were performed on the adjacent disk extracted from the same ingot, which confirmed the identical grain orientations in the two disks. An average difference in Bunge Euler angles [33] of 0.3 ± 0.1°, 0.2 ± 0.2° and 0.9 ± 0.4° for ϕ_1, Φ, and ϕ_2, respectively, was measured between the two disks, for three locations, which is consistent with the angular resolution limits of the method.

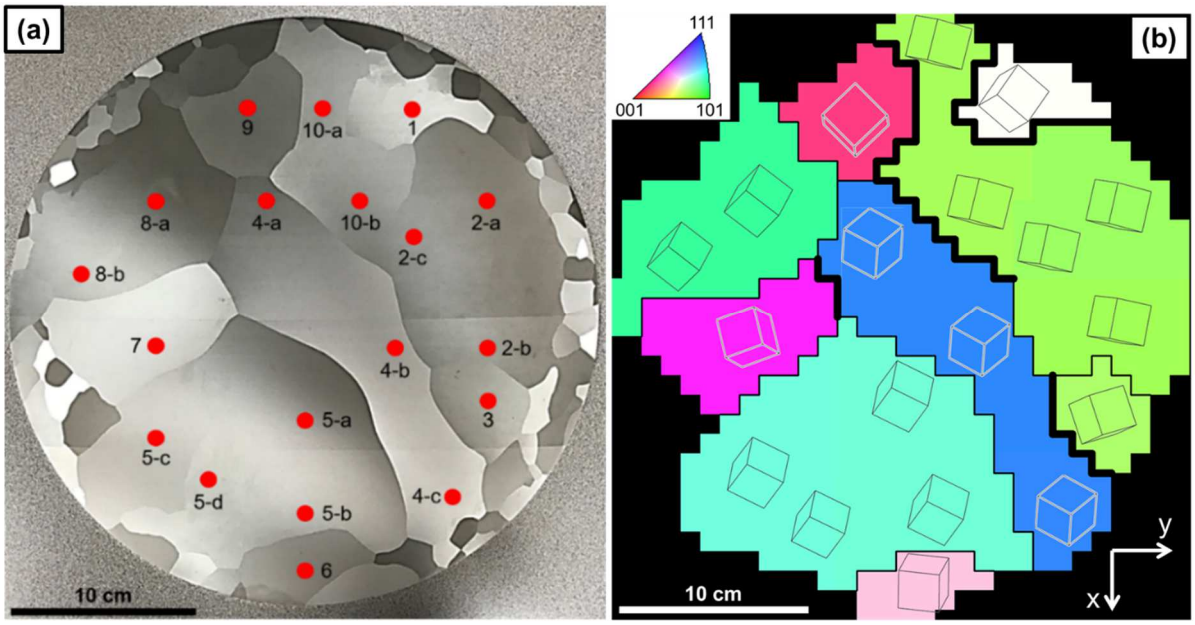

Figure 1: (a) Red points show locations where orientation measurements were performed and (b) normal direction orientation map of the 10 grains with unit cells showing crystal orientation; heavy lines identify coincidence site lattice (CSL) boundaries, and reference x and y directions are labeled.

2.3 Selection of Tensile Orientations

Tensile orientations were selected following a methodology based on the Schmid law developed for large crystals with one degree of freedom. The Schmid factor (SF) of the 24 slip systems in the $\{110\}\langle 111\rangle$ and $\{112\}\langle 111\rangle$ families were calculated for each grain in all possible in-plane tensile orientations. Specimen orientations were selected based upon 5 different conditions: (1) high ($>$ 0.49) and dominant SF in the $\{110\}$ system, (2) high and dominant SF in the $\{112\}$ system, (3) similar SF for both systems, (4) low ($<$ 0.4) SF for both systems, and (5) reproducibility of properties from adjacent samples with the same tensile direction, as well as nominally the same tensile axis obtained in different grains. Figure 2 shows the tensile and compression orientations of all cut specimens. The coloring of each specimen represents the crystallographic direction parallel to the tensile/compression axis in accordance with the inverse pole figure (IPF) shown in the top right corner of Figure 2a. The use of color identifies specimens with similar loading orientations obtained from different grains (having different cutting angles). Figure 2b shows the tensile axis crystallographic directions of the specimens (black markers) and the surface normal direction of each grain (grey markers) on the IPF. The specific selection of orientations includes multiple specimens for the five conditions previously described to ensure that the results are transferrable to disks with different grain orientations.

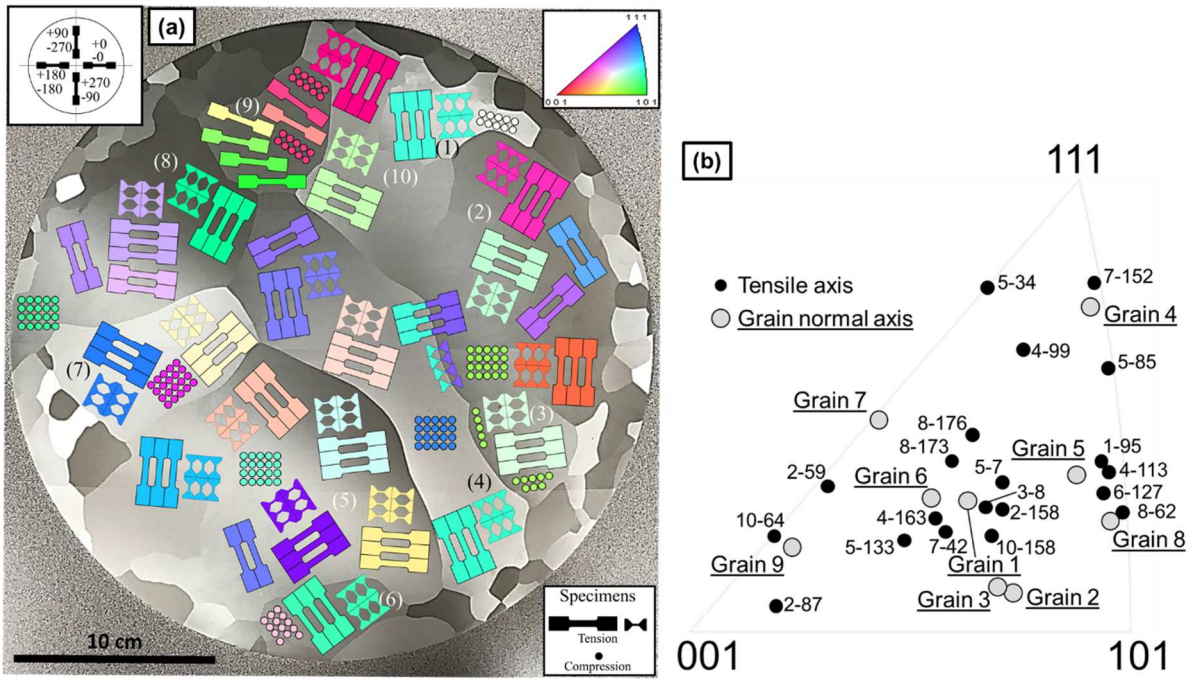

Figure 2: (a) Layout of tensile and cylindrical compression specimens for low and high strain rate tests and (b) inverse pole figure of the tensile axis (black markers) and grain normal axis (grey markers) orientations of all the specimens studied.

The following specimen nomenclature is used throughout this article: grain number-rotation angle, e.g. 4-113 stands for grain 4 and a 113° counter-clockwise rotation angle from the horizontal (y) axis. Table 1 provides the specimen number, the three Bunge Euler angles (the sample tensile direction is given by ϕ_1 and the original surface normal ∥ Z is unchanged for specimens from the same grain), the plane, Burgers vector, and Schmid factors of the two dominant systems for all tensile specimens.

Table 1: Tensile specimen label, lattice orientation relative to the coordinate system of Figure 1b, and the two dominant Schmid factors (m_1 and m_2) with their respective slip systems. QS and D stand for quasi-static and dynamic tests.

Specimen	ϕ_1 (°)	Φ (°)	ϕ_2 (°)	Plane 1	b_1	m_1	Plane 2	b_2	m_2	Tests
1-95	-65	148.7	158.1	$(\bar{1}\bar{1}2)$	[111]	0.497	$(\bar{1}01)$	[111]	0.438	QS, D
2-59	294	146.2	185.6	$(2\bar{1}\bar{1})$	$[\bar{1}\bar{1}\bar{1}]$	0.471	$(\bar{1}01)$	[111]	0.459	QS, D
2-87	266	146.2	185.6	$(\bar{2}\bar{1}1)$	$[1\bar{1}\bar{1}]$	0.496	(211)	$[\bar{1}\bar{1}1]$	0.483	QS, D
2-158	195	146.2	185.6	$(1\bar{1}0)$	$[\bar{1}\bar{1}\bar{1}]$	0.484	$(2\bar{1}1)$	$[\bar{1}\bar{1}1]$	0.479	QS, D
3-8	16.3	147.7	186.8	$(1\bar{1}0)$	$[\bar{1}\bar{1}1]$	0.487	$(2\bar{1}1)$	$[\bar{1}\bar{1}1]$	0.473	QS, D
4-99	-13	130.7	124.8	$(2\bar{1}1)$	$[\bar{1}\bar{1}1]$	0.436	(101)	$[\bar{1}\bar{1}1]$	0.413	QS, D
4-113	-27	130.7	124.8	$(2\bar{1}1)$	$[\bar{1}\bar{1}1]$	0.497	$(1\bar{1}0)$	$[\bar{1}\bar{1}1]$	0.438	QS, D
4-163	-77	130.7	124.8	$(0\bar{1}1)$	[111]	0.495	$(\bar{1}\bar{1}2)$	[111]	0.450	D
5-7	46.3	129.3	163.7	$(1\bar{1}0)$	[111]	0.479	$(1\bar{2}1)$	[111]	0.477	QS, D
5-34	19.3	129.3	163.7	$(1\bar{2}1)$	[111]	0.377	$(2\bar{1}1)$	$[\bar{1}\bar{1}1]$	0.373	QS, D
5-85	-31.7	129.3	163.7	$(\bar{2}\bar{1}1)$	$[1\bar{1}\bar{1}]$	0.464	(110)	$[1\bar{1}\bar{1}]$	0.403	QS, D
5-133	-79.7	129.3	163.7	$(\bar{1}01)$	[111]	0.497	(101)	$[\bar{1}\bar{1}1]$	0.454	QS
5-176	-122.7	129.3	163.7	$(1\bar{1}0)$	[111]	0.500	(110)	$[1\bar{1}\bar{1}]$	0.468	D

6-127	114	152.1	154.6	$(\bar{1}\bar{1}2)$	[111]	0.499	$(0\bar{1}1)$	[111]	0.443	QS, D
7-42	109	152.6	134.2	$(0\bar{1}1)$	[111]	0.496	$(\bar{1}\bar{1}2)$	[111]	0.454	QS, D
7-152	-1.0	152.6	134.2	$(1\bar{1}2)$	$[\bar{1}11]$	0.408	$(0\bar{1}1)$	$[\bar{1}11]$	0.354	QS, D
8-62	-17.5	132.8	168.2	$(\bar{2}11)$	$[1\bar{1}1]$	0.500	$(\bar{1}01)$	$[1\bar{1}1]$	0.434	QS, D
8-107	-62.5	132.8	168.2	$(\bar{1}01)$	[111]	0.445	$(\bar{1}\bar{1}2)$	[111]	0.443	QS
8-176	-131.5	132.8	168.2	$(1\bar{1}0)$	[111]	0.465	$(1\bar{2}1)$	[111]	0.455	QS, D
10-64	286.4	147.6	185.1	$(2\bar{1}1)$	$[\bar{1}\bar{1}1]$	0.498	$(\bar{1}01)$	[111]	0.450	QS, D
10-158	192.4	147.6	185.1	$(1\bar{1}0)$	$[\bar{1}\bar{1}1]$	0.490	$(2\bar{1}1)$	$[\bar{1}\bar{1}1]$	0.474	QS, D

2.4 Specimen Geometries, Cutting and Surface Preparation

All specimens were cut using wire electrical-discharge machining (EDM) based upon the horizontal alignment mark visible in Figure 1a. This technique was preferred to reduce specimen work hardening, waste, and for its high accuracy. Tensile specimens were later cut in half through their thickness using the same technique to double the number of specimens available for testing. The resulting average thickness was 1.76± 0.25 mm. The geometry and main dimensions of the specimens used for the quasi-static, intermediate, and high strain rate tests are presented in Figure 3. The shorter specimen geometry, shown in Figure 3a, was designed at Arizona State University (ASU) for high strain rate tests (~1000 s^{-1}) and previously used for other materials [34]–[36]. The tensile specimen in Figure 3b was designed based on the ASTM E8 subsize specimen and further miniaturized by a factor of approximately two [37]. The geometry of the specimens could influence the results, particularly in the post-necking regime, since the stress state is no longer uniaxial. Therefore, the flow stress for different strain rates is compared at a low strain of 0.05 to ensure uniaxial stress in both geometries and only the longer specimen geometry is used to compare the strain to failure between different strain rates. Tensile specimens from grain 5 were given a brief BCP etch to remove the EDM recast layer to allow for slip trace observations after the tests. An average of 44 μm was removed on all sides of those specimens, resulting in a mirror finish surface.

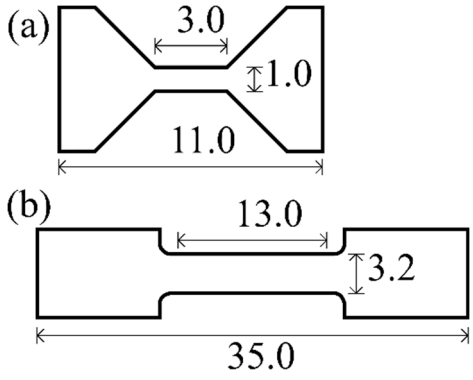

Figure 3: Geometry and main dimensions (in mm) of the tensile specimens used for the tests with (a) split Hopkinson bars and (b) at low and intermediate strain rates.

2.5 Tensile Tests

Quasi-static (QS) tensile tests were performed at room temperature and at constant crosshead speeds of 0.1, 1, 10, 50, or 100 mm/min, resulting in nominal strain rates of $1.3x10^{-4}$, $1.3x10^{-3}$, $1.3x10^{-2}$, $6.4x10^{-2}$, and $1.3x10^{-1}$ s^{-1} using a screw-driven table-top universal testing machine (Instron

4302) at Michigan State University (MSU). No extensometer was used, but the strain in the gage section was measured by digital image correlation (DIC) on three different specimens and a modulus correction was used on all other specimens to correct for the stiffness of the machine and the grips from the measured crosshead displacement.

Tensile tests at average intermediate nominal strain rates of 1.12, 7.95, and 94.9 s^{-1} were performed at room temperature at Imperial College London with an Instron VHS servo-hydraulic universal testing machine. A lost motion rod system was used to ensure a constant velocity during the tests [38]. Specimens with the same geometry as the QS tests were used. All specimens were painted on one side with a uniform white layer and black speckles for DIC. The other side of the gage section was painted with a matte black layer to obtain a high and uniform emissivity for temperature measurements at 200 Hz with an uncooled infrared camera (FLIR A655sc). A Phantom Miro M310 high-speed camera was used at acquisition rates of up to 65,000 frames per second for the DIC used to measure the displacement between two points at the extremities of the gage length.

Split Hopkinson tensile bar (SHTB) tests were conducted at room temperature at ASU. The striker, input and output bars of the in-house SHTB system were made of maraging steel [39]–[42]. The input and output bars were 0.5″ (~12.7 mm) in diameter. Thin copper rings were used as pulse shapers to obtain nearly constant strain rate deformation in the single crystals [43]. Strains were acquired at a frequency of 2 MHz. A few specimens were also painted for DIC measurements using a Photron FASTCAM SA-Z to acquire images at 100,000 frames per second.

2.6 Microstructure Analysis

The microstructure and grain orientation of the longitudinal cross-section of selected specimens was investigated using electron backscatter diffraction (EBSD) mapping (ZEISS FEG-SEM Sigma and Oxford Instruments' Nordlys detector). Specimens were cut lengthwise using a diamond wire saw (Well Diamond Wire Saw Series 3000). The cut specimens were cold mounted and polished with silicon carbide (SiC) papers up to P4000 grit. Finally, manual polishing with 3 and 1 μm diamond suspension solutions and vibratory polishing (Buehler Vibromet 2) with a colloidal silica solution for more than 2 hours was performed. A low geometrically necessary dislocation (GND) density and high confidence index in undeformed regions of EBSD scans indicated that the polishing process was effective. All EBSD analyses were performed using the free MATLAB toolbox MTEX [44].

3 Results and Discussion

3.1 Effect of Orientation

Figure 4a and b show engineering stress–strain curves for 17 and 18 different samples deformed in tension at nominal strain rates of 1.28×10^{-3} and 1.28×10^{-2} s^{-1}, respectively. Tensile axis IPF colors are used on a gray background to identify trends related to initial orientation. A minimum of two tests were performed for each orientation, but only one curve is presented for orientations that were highly repeatable. Large differences in hardening behavior are observed between the different orientations, for both quasi-static strain rates. Since plasticity in niobium single crystals is related to

the thermal activation of dislocations gliding on slip planes, the anisotropy results from the activation and interaction of different slip systems.

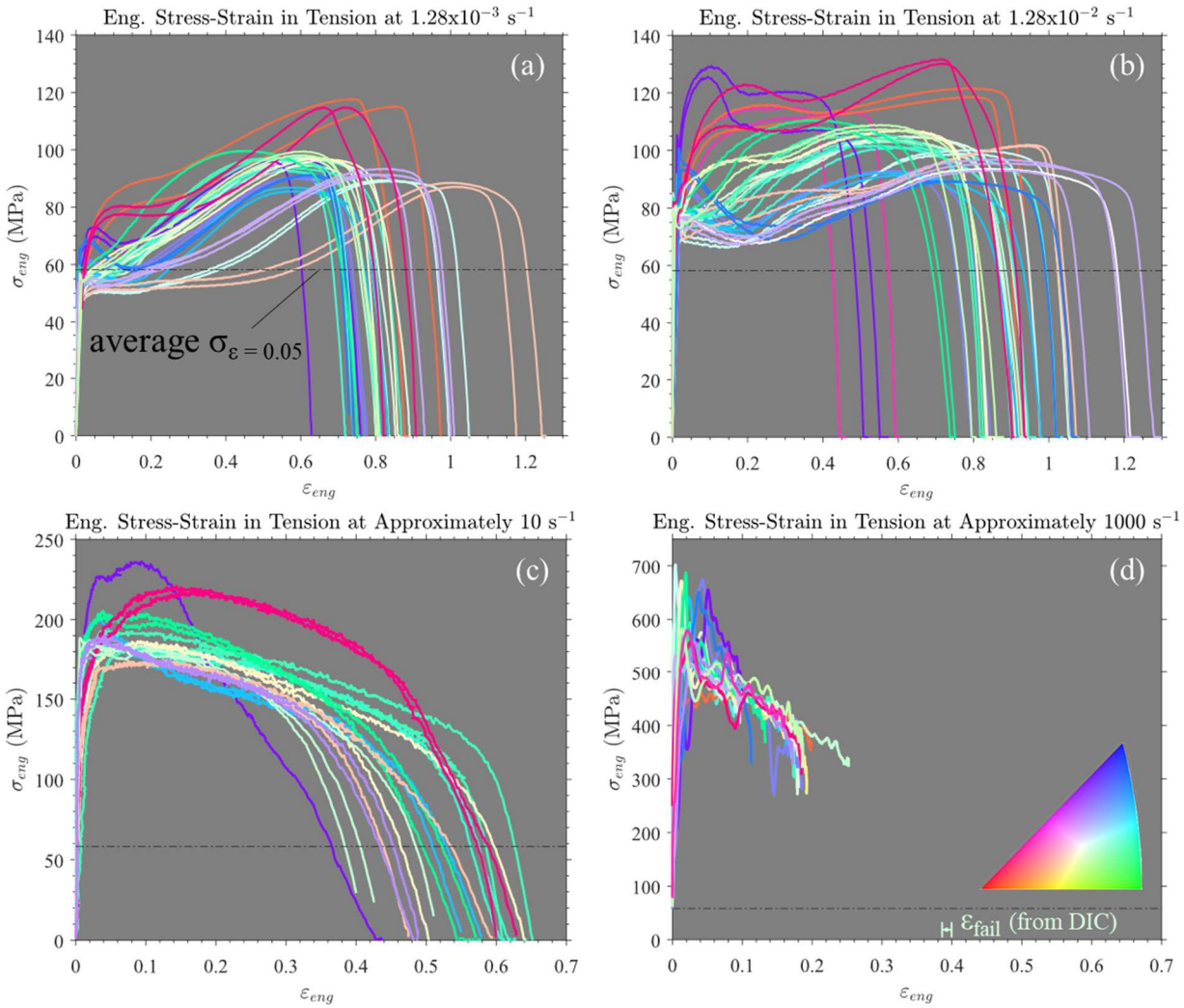

Figure 4: Engineering stress–strain curves of tensile specimens with different crystallographic orientations at nominal strain rates of (a) 1.28x10^{-3}, (b) 1.28x10^{-2}, approximately (c) 10, and (d) 1000 s^{-1}, colored by initial crystallographic tensile axis (see IPF inset). Split Hopkinson results are not up to fracture, since only the first strain wave was used for analysis. However, the strain to failure of specimen 3-8, measured with DIC, is plotted for reference. The black dash-dotted line represents the mean flow stress at 0.05 strain at a strain rate of 1.28x10^{-3} s^{-1} to enable comparison between the different stress scales.

A comparison of Figure 4a and b shows an increase in yield stress with increasing strain rate. An initial strain softening is observed for most of the samples deformed at 1.28x10^{-2} s^{-1}, but is only visible for a few samples at the lower strain rate.

Figure 4c shows engineering stress–strain curves for 9 different tensile orientations deformed at an intermediate nominal strain rate of approximately 10 s^{-1}. All curves show softening after yield and different softening behaviors, especially for orientations near [001] and [111]. Temperature increases of approximately 40 and 85°C were measured at the onset of necking and in the neck before rupture, respectively. These values are low compared to the melting point of niobium

(~2,477°C). Moreover, as softening is observed directly after yielding, it cannot be attributed only to adiabatic heating effects.

3.1.1 Hardening Stages

Stress–strain curves of single crystals are often described with three hardening stages. Stage I, also called *easy glide*, has a low strain hardening rate and one primary slip system is active. Stage II starts with the increasing activation of secondary slip systems and the interaction of primary and secondary dislocations causes a higher and nearly constant hardening rate. Finally, stage III features a decreasing hardening rate and a saturating flow stress due to the dynamic annihilation of dislocations by cross-slip. The tensile specimens deformed at the lowest strain rate of 1.28×10^{-3} s^{-1} and with the lowest yield stress all show the three hardening stages, as shown in Figure 4a. At a strain rate of 1.28×10^{-2} s^{-1} (Figure 4b), most tensile orientations exhibit a qualitatively very similar three-stage hardening behavior as observed at 1.28×10^{-3} s^{-1}. Consistent with this observation, Gnäupel-Herold et al. [22] observed three stages in their tensile tests at strain rates of 10^{-4} s^{-1} or smaller with different hardening rates and strain intervals between the stages for different orientations. As demonstrated for a particular tensile orientation in Figure 7, the presence of a clear stage I and II hardening gradually disappears at deformation rates between 10^{-1} and 10 s^{-1} (see also Figure 4c). This implies that multiple slip systems are activated after yield. Such behavior is not unexpected, as it is likely that the initially most stressed slip system gradually reaches the limit of its capacity (given by mobile density and maximum dislocation velocity) to accommodate ever higher imposed deformation rates. Therefore, part of the imposed (total) deformation rate results in increasing elastic deformation until further slip systems become sufficiently active at higher stress. The immediate (in terms of plastic strain) interaction of dislocations on intersecting slip planes then results in the absence of stage I hardening.

The activation of multiple slip planes directly after yield was not directly observed because it would have required slip trace analysis, such as done in-situ by Kang et al. [20] for low strain rates up to 2.2×10^{-4} s^{-1}. The disappearance of stage I for increasing strain rate up to about 10^{-1} s^{-1} was also observed by Mitchell et al. [11].

The absence of stage II for strain rates greater or equal to ~10 s^{-1}, shown in Figure 4c and d, is probably due to a combination of different parameters: (1) the annihilation of dislocations by cross-slip, which is linked to the motion of dislocations on multiple slip systems (e.g. cross slip from {110} to {112} planes, and *vice versa*), (2) diffuse necking happened sooner, as indicated by the maximum flow stress at a lower strain in the stress-strain curves for higher strain rates and, and (3) thermal softening. These conclusions are based on the changes in the hardening and softening behavior exhibited in the stress-strain curves and especially the reduction of anisotropy at the highest strain rate (if more slip systems are active, then deformation is more uniform). Mitchell and Spitzig [45] studied the mechanical properties of Ta single crystals deformed at different strain rates and observed a similar behavior. They suggested that the hardening effects were “masked by unstable plastic flow and rapid necking” due to the initially high flow stress at high strain rate or low temperature.

3.2 Split Hopkinson Tensile Bars

Figure 4d shows the tensile properties of niobium single crystals deformed in 19 different crystallographic orientations with split Hopkinson bars at strain rates close to 10^3 s^{-1}. The high strain rate tests show a significant increase in the 500–650 MPa yield stress compared to the 50-70 MPa quasi-static tests. Moreover, the anisotropy is significantly reduced as the flow curves are much more similar for many orientations. This could also be explained by the combined effects of activation of multiple slip systems to accommodate for the imposed plastic strain at high rate, adiabatic heating effects, and strain heterogeneity from the split Hopkinson bar test (see section 3.3). The flow stress in all orientations reduces directly after yielding and through all the plastic domain. However, this apparent softening behavior does not necessarily imply a plastic flow localization. The high strain-rate sensitivity of the material may contribute to stabilize the plastic flow and delay the onset of localized necking [46], [47]. The high-speed camera observation did not reveal any occurrence of localized necking during the loading induced by the first incoming wave, but significant strain heterogeneities due to sample length and the nature of the split Hopkinson bar tests, as shown in Figure 6 [48], [49].

The maximum engineering strains measured during the SHTB tests are around 0.2. This value is however not the strain at fracture, but the strain of the specimen after deformation from the first incoming strain wave. The use of a high-speed camera showed that specimens usually failed after the third strain wave. Since the second and third waves are the consequences of the reflection of the initial wave at the end of the bars, the signal becomes difficult to analyze and consequently mechanical properties are only presented for the first wave.

Due to the dynamic nature of the tests, adiabatic heating from dissipation of mechanical energy into heat is expected. If significant enough, the concentration of heat in the neck leads to a strength reduction. In-situ measurements of the temperature were performed on single crystals deformed at 1, 10 and 100 s^{-1}. An average maximum temperature of 85 °C was measured in the necks before failure for three specimens deformed at 10 s^{-1}. The temperature is expected to be higher for the tests performed at 1000 s^{-1}. The experimental results of Mitchell et al. [11] showed that the temperature dependence of flow stress of niobium single crystals is low for temperatures above 298 K. Moreover, the apparent softening observed in the SHTB tests cannot be attributed only to adiabatic heating effects as it takes place directly after yield. A decrease in the peak force strain and a decrease in hardening at high strain rates is often observed for BCC polycrystalline metals, see Peroni and Scapin [50] for niobium and Hoge and Mukherjee [51] for tantalum. This phenomenon has been analyzed by Ghosh [47] and Zerilli and Armstrong [52]. The strain rate sensitivity of BCC materials is almost independent on the dislocation density and the plastic strain for polycrystalline materials [53]. In other words, an increase in strain rate causes an overstress with a magnitude independent on the plastic strain level. For this reason, the maximum force condition ($\frac{\partial \sigma}{\partial \epsilon} = \sigma$ with σ being the true flow stress and ϵ the true strain) is met at a smaller strain when the strain rate is increased.

The observation made in section 3.1.1 on the activation of multiple slip systems after yield for higher strain rates is extrapolated to the dynamic tests. Since anisotropy is enhanced by the activation of limited slip systems, the activation of multiple slip systems for all crystallographic orientations leads to more uniform strains and similar flow behavior for different orientations.

3.3 Spatial Heterogeneity of Strain

To examine the hardening behavior observed for three different samples, digital image correlation (DIC) was used to measure the distribution of total strain in the specimens. Figure 5 shows the strain distribution at six different engineering strains in specimen 7-152, with a tensile orientation near the [111] direction, deformed at a nominal strain rate of 1.28×10^{-2} s^{-1}. Strain maps are numbered with their corresponding strains to show the strain distribution in the softening and hardening regimes at the macroscopic scale. Plots of the total tensile strain distribution in the gage section of each strain map are presented for quantitative comparison in the top right of Figure 5. Pictures 3 and 4 show a region of high strain at the bottom of the specimen, indicating the onset of localized necking with thinning through the specimen thickness. However, the specimen did not fail in this region because it started to harden and did not deform further at a global strain of 0.25. Pictures 5 and 6 show more uniformly distributed total strain in the gage length, which corresponds to the hardening section of the curve.

The activation of different slip systems due to a rotation of the crystal could explain the transition from softening to hardening, since crystal rotation was measured with EBSD orientation maps. A change in the interaction of dislocations with each other or with interstitial atoms is also likely responsible for the change in hardening rates. An expanding band, similar to a Lüders band in steel, was not observed with DIC, but the successive increase in strain in adjacent regions represents a strain propagation band in the specimen.

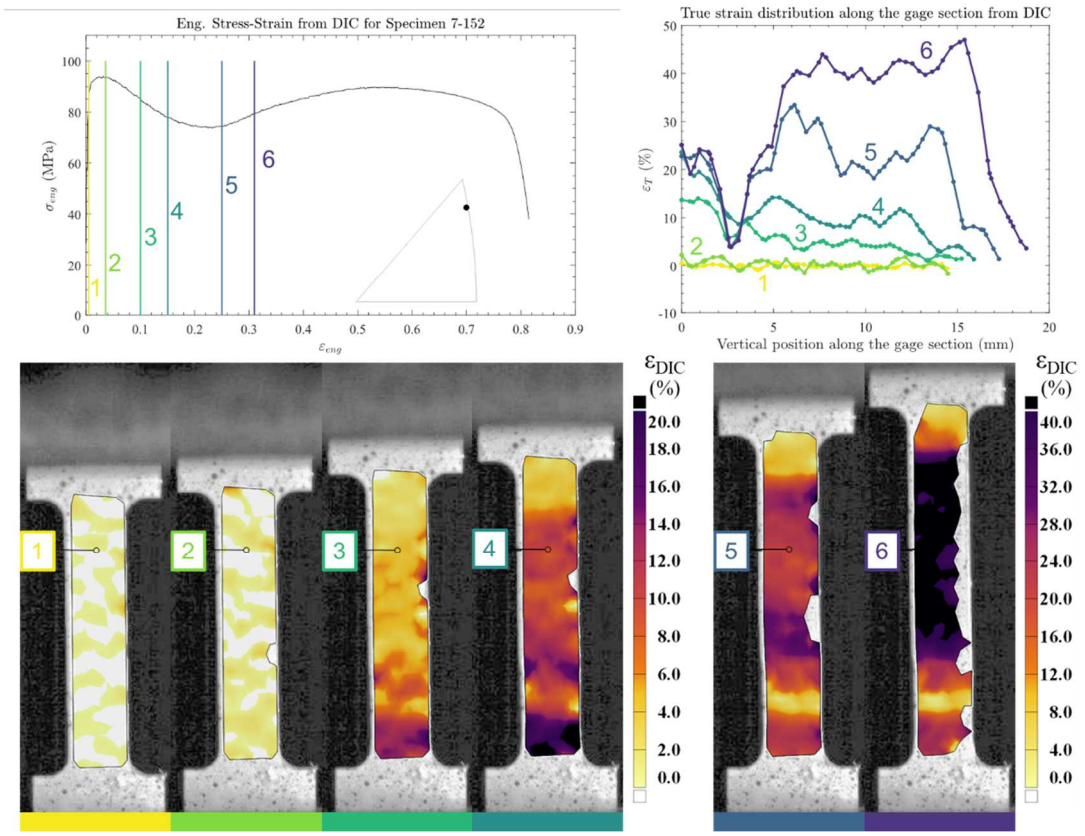

Figure 5: Strain localization of a specimen in the [111] orientation deformed at 1.28×10^{-2} s^{-1}. (The strain reduction in the neck in 5 and 6 is not physical, but an artefact of the 2D DIC method.)

Figure 6 shows strain localization in four specimens deformed at high strain rates with split Hopkinson tensile bars with different crystallographic orientations. Strain heterogeneities appears rapidly in the specimen. It is also interesting to observe that the region where the strain reaches its maximum is generally not located at the center of the specimen. This phenomenon is probably related to wave propagation effects [48], [54]. Moreover, the rather short length of the specimens used in the slip Hopkinson bar tests probably also contributes to the strain field heterogeneity [48], [49]. However, the heterogeneity of the strain distribution does not grow very much during the deformation of the specimen and localized necking is not reached during the first wave loading (see section 3.2).

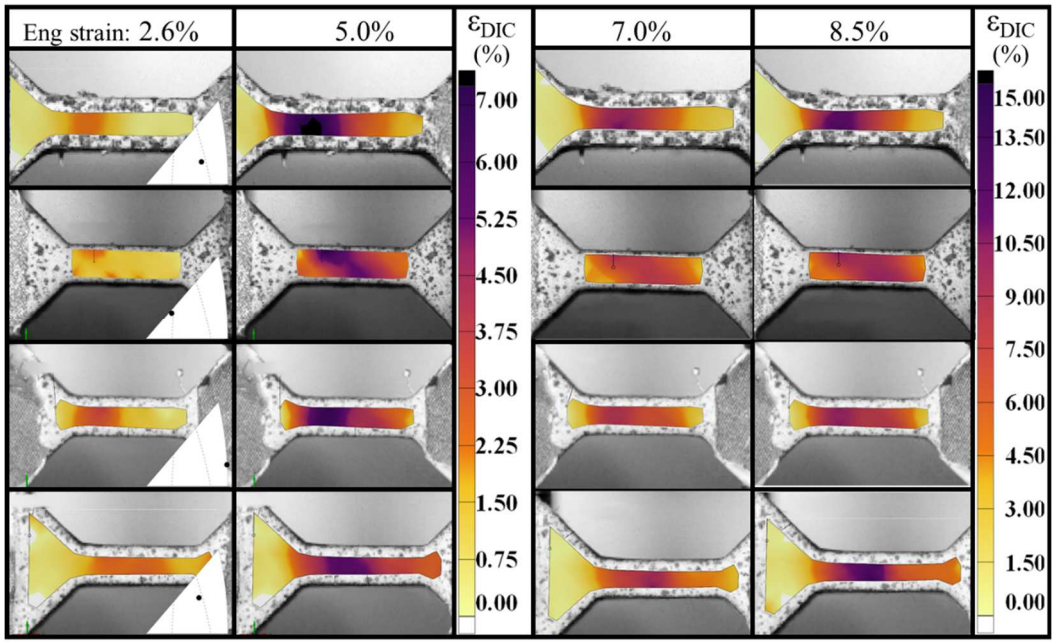

Figure 6: DIC strain maps of four specimens deformed at high strain rates ($\sim 1000\ s^{-1}$) showing strain localization at low engineering strains. The initial tensile direction for each specimen is shown as dots on the inverse pole figure in the lowest strain image of each sample.

3.4 Effect of Strain Rate

The effect of strain rate on crystals with tensile directions near the center of the tensile axis IPF (crystals 2-158 and 3-8), for nine different strain rates is compared. Because the two orientations are very similar, results for both crystals are presented on the same plot to determine the strain rate sensitivity. Figure 7 combines the stress–strain curves for both orientations across all strain rates.

Figure 7 reveals a systematic increase in flow stress with increasing strain rate. The elongation to failure is maximal at about 6.41×10^{-2} s^{-1}, and drops quickly with increasing strain rate as the work hardening rate becomes level or negative. A larger dispersion in fracture strain occurred for the tests performed at 1 and 10 s^{-1}, where adiabatic heating begins to be measurable, which may lead to preferential strain near a neck [55]. This transition also corresponds with a notable yield drop at about 120 MPa ($\sim 10^{-1}$ s^{-1}). The lack of a yield drop is probably caused by longer times for thermal activation of dislocation motion and hence a higher probability for dislocation detachment from pinning sites. Pinning is more dominant when there is less opportunity for thermally assisted detachment, so that the upper yield point (and its disappearance at higher rates) represents a locally saturated interstitial atom concentration in the dislocation core [41], [56]. Barely noticeable yield drops, less than 1 MPa in magnitude, were also observed by Gnäupel-Herold et al. [22] for different orientations, but for tensile tests performed at strain rates of 10^{-4} s^{-1} or lower.

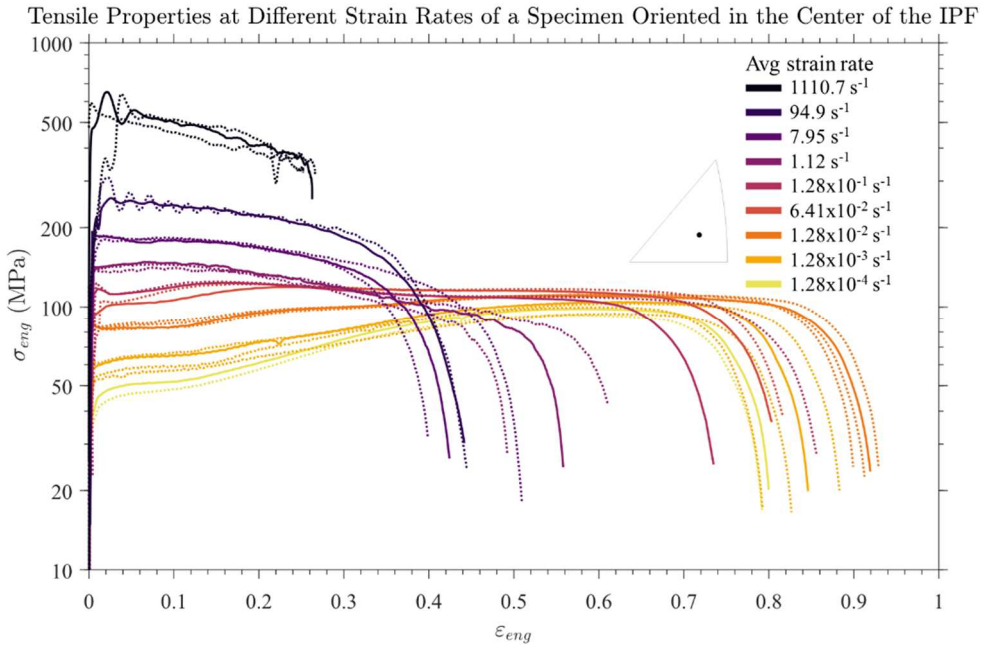

Figure 7: Tensile engineering stress–strain curves with a logarithmic stress scale for strain rates from 1.28×10^{-4} to approximately 1000 s^{-1} on specimens 2-158 and 3-8 with a crystallographic orientation near the center of the IPF. (Dotted lines are repeat measurements for the same strain rate.)

To compare properties of specimens with similar dislocation substructures at the different strain rates, strain rate change tests are often conducted to calculate the strain rate sensitivity. In this study, the strain rate sensitivity was calculated for engineering strains of 0.05 since no rate change tests were performed and stress equilibrium in split Hopkinson bars is often not reached at strains lower than 0.05 [57]. The flow stress in tension for the same crystal orientation as function of strain rate across eight orders of magnitude is presented in Figure 8a in light green together with seven additional crystal orientations colored according to their respective tensile axis IPF colors and tested over three orders of magnitude in strain rate. The strain rate sensitivity of the specimen near the center of the tensile axis IPF deformed at room temperature, $m = (\partial \ln \sigma / \partial \ln \dot{\varepsilon})_{\varepsilon=0.05} = 0.14$, is consistent over all but the highest strain-rate data. The resistance from the inertial forces opposing the deformation were estimated to be about 12 MPa [58]. This contribution is too small to explain the deviation at the highest rate [58]. Figure 8a also provides a comparison with the literature. Despite different single crystal processing techniques and purity levels, the flow stresses at strain rates of the same order of magnitude are similar.

Figure 8b shows a reduction of the strain to failure with decreasing strain rates below 10^{-2} s^{-1} for different orientations. A similar result was obtained by Mitchell et al. [11] at a similar strain rate and by Ricker et al. for tests at 10^{-5} and 10^{-6} s^{-1} and was explained by the increased interaction time between dislocations and mobile hydrogen interstitial atoms at the lowest strain rate [23], i.e. dynamic strain aging. The opposite trend is observed for the specimens deformed at intermediate strain rates, where the strain to failure is lower compared with the quasi-static specimens, for all orientations.

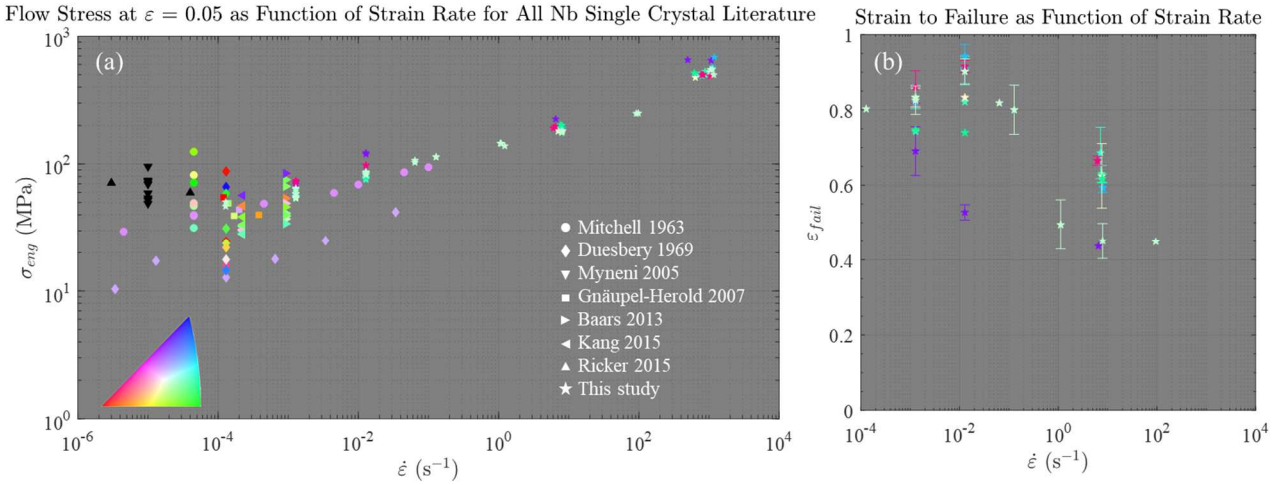

Figure 8: (a) flow stress at ε = 0.05 from the literature and this study with symbols colored by the tensile axis (black if not known) and (b) strain to failure across eight orders of magnitude of strain rate for an orientation near the center of the tensile axis IPF (specimens 2-158 and 3-8) and for three orders of magnitude of strain rate for 7 additional orientations. (Error bars are not plotted when the standard deviation is smaller than the marker size or only one test was performed.)[2]

3.5 Activation Volume

Short range dislocation barriers, such as the Peierls–Nabarro stress, point defects (e.g. vacancies and self-interstitials) and other dislocations intersecting the slip plane, are temperature and strain rate dependent [60]. The resistance to dislocation motion is then dependent on a thermal term and the identification of the dominant thermally activated mechanism is possible by calculating the activation volume [60]. The activation volume is defined as the derivative of the activation enthalpy with respect to the thermal component of the stress and is calculated as

$$v^* = \frac{\sqrt{3}k_B T}{\sigma}\left(\frac{\partial \ln \dot{\varepsilon}}{\partial \ln \sigma}\right)_T$$

where k_B is the Boltzmann constant, T is the absolute temperature and $\partial \ln \dot{\varepsilon} / \partial \ln \sigma$ is the inverse of the strain rate sensitivity. Mitchell et al. calculated activation volumes for high-purity niobium single crystals using the strain rate sensitivity at yield, and the activation volumes of 75 and 30 b^3 were obtained at strain rates of 4.5×10^{-6} and 1×10^{-1} s^{-1}, respectively [11], [61]. Using the same method, the activation volumes are calculated for specimens 2-158 and 3-8 for all strain rates using constant ($m = 0.14$) and rate-specific strain rate sensitivities at ε = 0.05 from Figure 8. Figure 9 shows excellent agreement between Mitchell et al. [11] and the present study, where v^* decreases from 60.6 b^3 to 2.6 b^3 with increasing flow stress. The decrease in activation volume in inverse proportion to the flow stress is consistent with a constant strain rate sensitivity and not uncommon for the range of strain rates studied. An increase in strain rate sensitivity at the highest strain rate, as shown in Figure 8, results in a higher rate of reduction of activation volume.

[2] The flow stress in Duesbery's study [14] was calculated assuming that the specimen geometry was the same as in the study of Mitchell [11] (tests performed at same laboratory and the difference in calculated axial stresses is similar to the difference in reported shear stresses). The flow stress in Myneni's study [59] required to extract data from two sources to obtain the load [59] and calculate the likely specimen cross-sectional area by extracting the stress of one specimen [21].

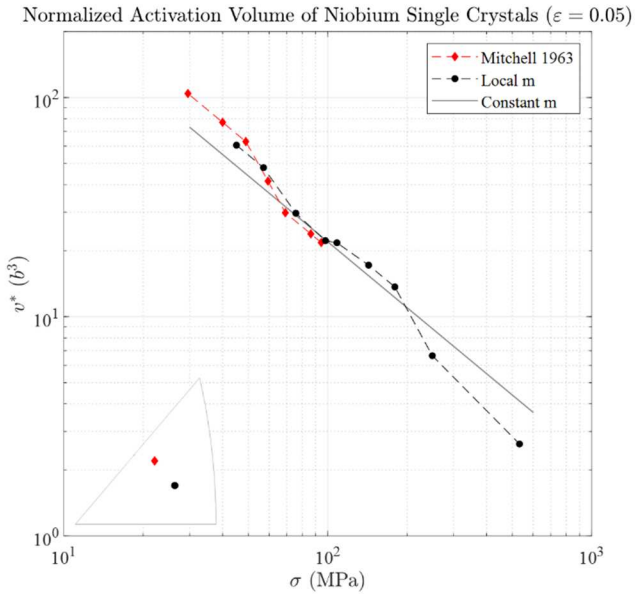

Figure 9: Activation volume as a function of the flow stress at ε = 0.05.

According to Conrad [60], the decreasing activation volume from quasi-static to dynamic rates corresponds to the thermal activation of two mechanisms observed in BCC metals: overcoming of the Peierls-Nabarro stress, which is probably responsible for the increase in flow stress at the higher strain rates [62], [63], and cross-slip, as observed by Duesbery et al. [13] in shear bands on the surface of deformed single crystals. The increasing activation volume with decreasing flow stress represents the volume over which thermal activation must operate to dissociate a dislocation from an interstitial pinned atmosphere.

3.6 Fracture Surfaces

Figure 10 compares top views of fracture surfaces of tensile specimens with three different initial tensile orientations and deformed at strain rates of 1.28×10^{-2} and approximately 1000 s^{-1}. The macroscopic specimen rotation is often similar at quasi-static and dynamic strain rates, as in specimens 2-158 and 7-152. However, the longer gage section and strain to failure in quasi-static specimens leads to a larger rotation, as shown for specimen 5-85 in Figure 10e.

Figure 11 shows secondary electron front and top views (viewing along the tensile axis) of fracture surfaces of tensile specimens with different crystallographic orientations deformed at approximately 1000 s^{-1}. For these specimens, the strain rate at rupture is expected to be lower than 1000 s^{-1} since fracture occurred after being deformed by the third strain wave passing through the bars, which had dissipated energy after each wave. All specimens show a ductile rupture with a chisel-edge profile. This is common for single crystals of high purity deformed at low strain rates [45], [64].

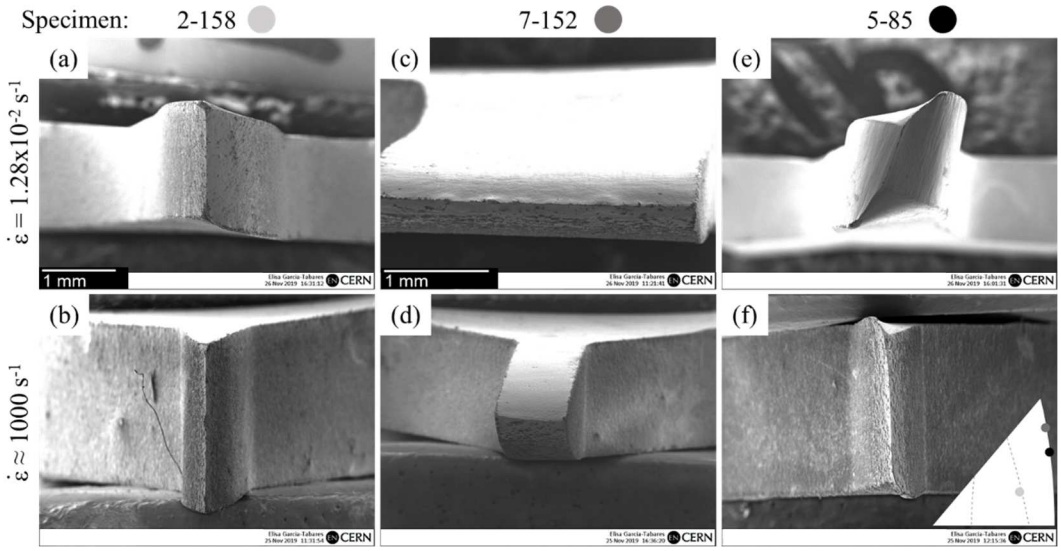

Figure 10: Secondary electron top views of rupture surfaces of specimens 2-158 (a, b), 7-152 (c, d), and 5-85 (e, f) deformed at quasi-static and high strain rates. The initial tensile direction for each specimen is shown as dots on the inverse pole figure in (f). (a, b, d, e, and f share the same scale bar.)

The number of active slip systems at rupture should influence the rupture surface morphology, i.e. the crystal rotation and neck geometry, such as the two- and four-fold symmetries observed in copper single crystals deformed at different temperatures by Simoto et al. [65]. Considerable variations in fracture surface morphology for specimens deformed at high strain rate are visible in Figure 11. However, no orientation-based trends in fracture surface edge rotation and length are observed. Specimens with initial tensile orientations in the center or on the [101]–[111] boundary of the tensile axis IPF showed both short and rotated (specimens 7-42 and 6-127), and long and straight (specimens 2-158 and 7-152) fracture surface edges.

3.7 Microstructural Analysis

Based on slip theories [26], all tensile BCC single crystal specimens should rotate toward the terminal stable [101] orientation. While no macroscopic rotation is observed for specimens 2-158 and 7-152 deformed at high strain rate in Figure 11, microscopic orientation rotations toward [101] were measured with EBSD.

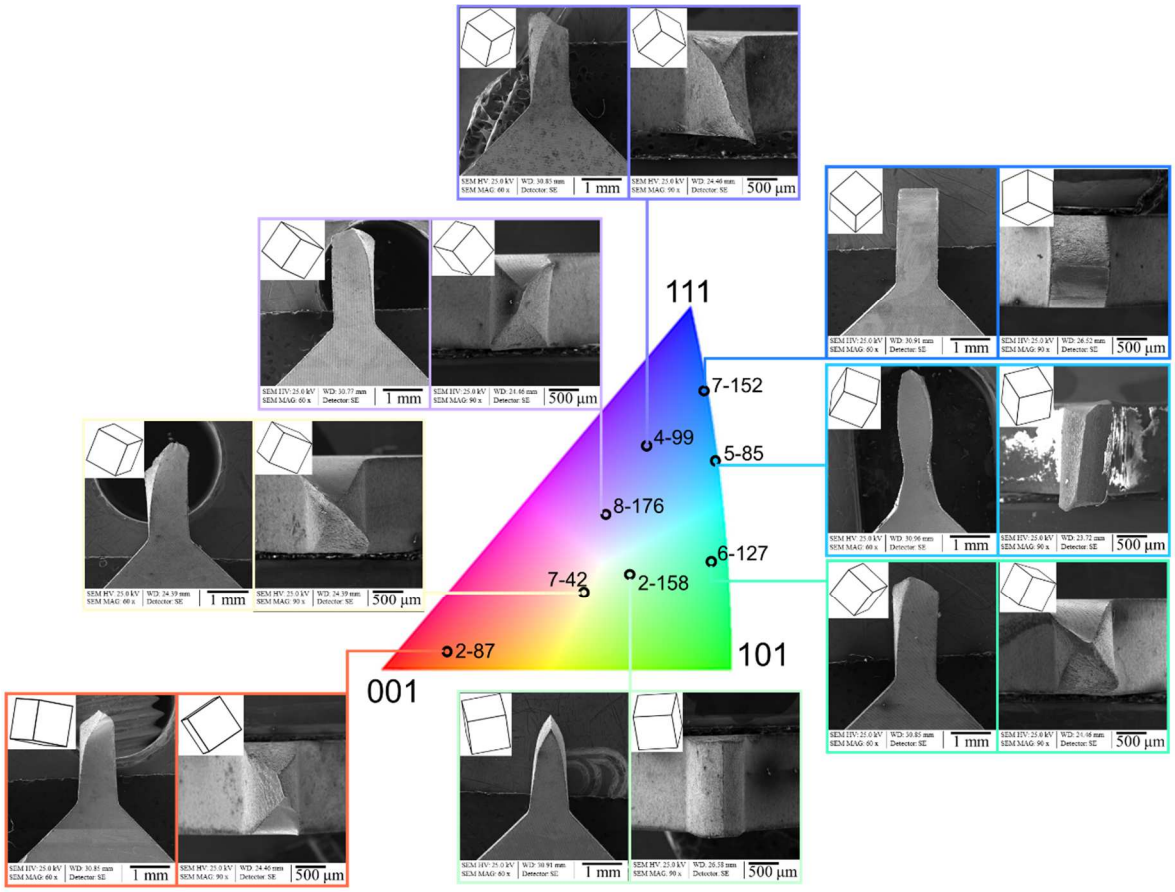

Figure 11: Fracture surface of niobium single crystals deformed at high strain rate in tension for six different orientations with unit cells of undeformed initial orientations normal to each view.

While stress anisotropy is reduced at dynamic rates the crystal rotation appears to be a macroscopic kinematic strain-driven process. The specimen dimensions, which affect the post necking behavior and consequently the strain-to-failure, could be the main factor influencing the extent of the rotation occurring in single crystals with the same orientation. The direction of the rotation should be the same for crystals with similar initial orientations as it is dictated by the active slip systems. EBSD measurements confirmed similar rotations for the quasi-static and dynamic specimens with the same initial tensile orientation, see Figure 12b and Figure 13b.

EBSD measurements were performed on polished cross-sections of low strain rate specimens to measure the change in crystal tensile orientation between the undeformed grip section and the fracture surface. Figure 12a shows the crystallographic orientation, in the tensile direction, and local average misorientation (LAM) maps for five different sections of a specimen with an initial orientation near the center of the IPF (white areas on the orientation maps are regions with poor pattern indexation and artifacts of polishing). The rotation occurs around the vector equal to the cross product of the slip plane normal and slip direction of the active slip system, which is approximately the out-of-plane direction in Figure 12a. This was observed for all specimens with no shear bands. A rotation toward the terminal stable [101] direction was measured for this orientation and three others shown in Figure 12b. An increase in GND density between the fixture and the fracture surface is evident in the local average misorientation map. Interestingly, the orientation in

the grip differs from the original orientation for few specimens and is likely caused by alignment errors during specimen cutting and measurements, and also because measurements were taken in a region of the grip where biaxial strain probably took place, as schematically shown in light red on a half-tensile specimen in Figure 12b and Figure 13b.

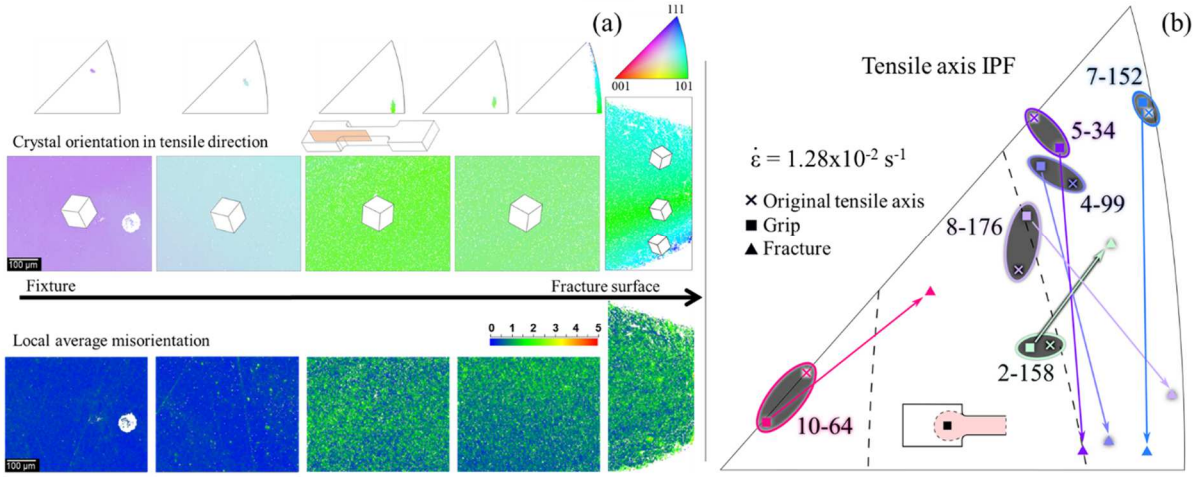

Figure 12: (a) EBSD orientation map in the tensile direction and misorientation of specimen 8-176 with an initial crystallographic orientation near the center of the IPF deformed in tension at 10^{-2} s^{-1}. (b) Orientations in the grip (square), near the fracture surface (triangle) and theoretical (crosses) for six specimens deformed at low strain rates. A half-specimen schematically shows the location of the grip measurement and possibly deformed region within the grip in light red.

Figure 13a shows EBSD scans for a specimen with the same tensile orientation as in Figure 12a, but deformed at high strain rate. In contrast to the quasi-static specimen that has a gradually increasing GND density from the fixture to the fracture, the dynamic specimen has a high GND density at the fracture surface and a low misorientation elsewhere. This is probably caused by the formation of a neck at a lower strain and a more intense straining in the neck region in the dynamic test. The deformation, and consequently the highest GND density, is then concentrated in the vicinity of the fracture surface. Similar observations in local misorientation distribution between low and high strain rate specimens were made for specimens 2-158 and 7-152.

The insets in Figure 13a show higher resolution maps (step size of 0.5 µm compared to 2 µm). Note that the bands of higher misorientation angle (~1–2°) converging at the fracture surface edge in the low-resolution scan are an artefact of the large step size and represent the overall specimen rotation. Figure 13b compares the crystal rotation from the grip to the fracture surface for three specimens deformed at high strain rate, which are similar to the rotations observed for the same orientations at low strain rate in Figure 12b, except for specimen 2-158 where the low strain rate rotation is toward the [111] direction.

Specimen number 5-34, which has a tensile axis where there are equally low Schmid factors for the {110} and {112} slip systems, showed the highest hardening and lowest elongation for the tensile tests at $1.28x10^{-2}$ s^{-1}. The specimen also showed shear bands on its top and bottom surfaces after deformation, as illustrated in the image of the sample in the top of Figure 14. An EBSD analysis confirmed that the bands at the surface were shear bands with very different crystal orientations as

shown by the contrasting colors in Figure 14. The heterogeneous slip behavior of the bands and the matrix resulted in a composite-like structure, which could account for the stress-strain curve with high hardening, associated with different slip directions in adjacent regions, and low ductility that results from instabilities caused by formation of grain boundaries during deformation, and hence, adjacent orientations that are relatively harder or softer.

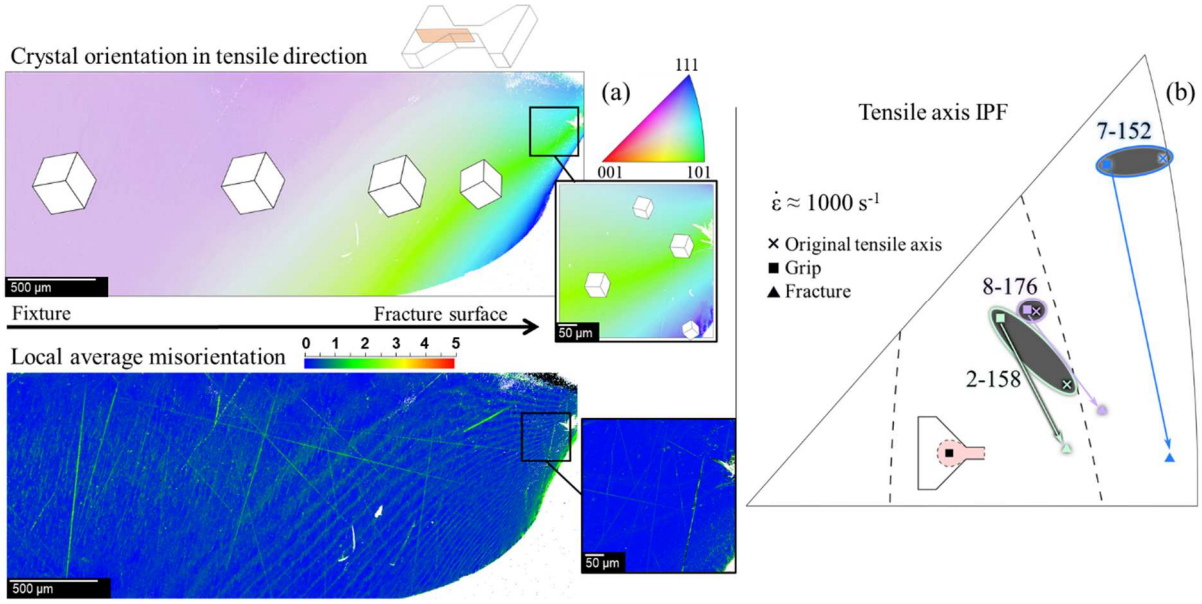

Figure 13: (a) EBSD orientation map in the tensile direction and misorientation of specimen 8-176 with an initial crystallographic orientation near the center of the tensile axis IPF deformed in tension at 10^3 s^{-1}. (b) Orientations in the grip (square), near the fracture surface (triangle) and theoretical (crosses) for three specimens deformed at high strain rates. A half-specimen schematically shows the location of the grip measurement and possibly deformed region within the grip in light red.

Shear bands were also observed in specimen 4-99, with an initial orientation close to specimen 5-34. The two slip systems with the highest Schmid factors in specimen 4-99 have similar resolved shear stresses on different slip planes sharing the same slip direction. This orientation also showed a low ductility and a high hardening rate. Softening shortly after yield was observed in the stress–strain curves of both specimens 4-99 and 5-34 and is likely caused by the formation of the shear bands [66], [67]. Baars et al. [18] also observed regions with distinct orientation splitting in specimens with the highest hardening and where slip is expected to occur in different <111> directions. Because some crystal orientations will deform in a manner that leads to orientation splitting, this can account for a wide range of ductility, such as observed in polycrystals with texture banding [68]. Clearly, it is important to be able to predict which crystal orientations are most likely to generate orientation splitting when considering formability of large grain material. However, this prediction is difficult to make since the initial orientation of specimens 4-99 and 5-34 are similar, with low Schmid factors, but the slip direction in the two slip systems with the highest Schmid factors were the same for 4-99, and different for 5-34 (which showed orientation splitting).

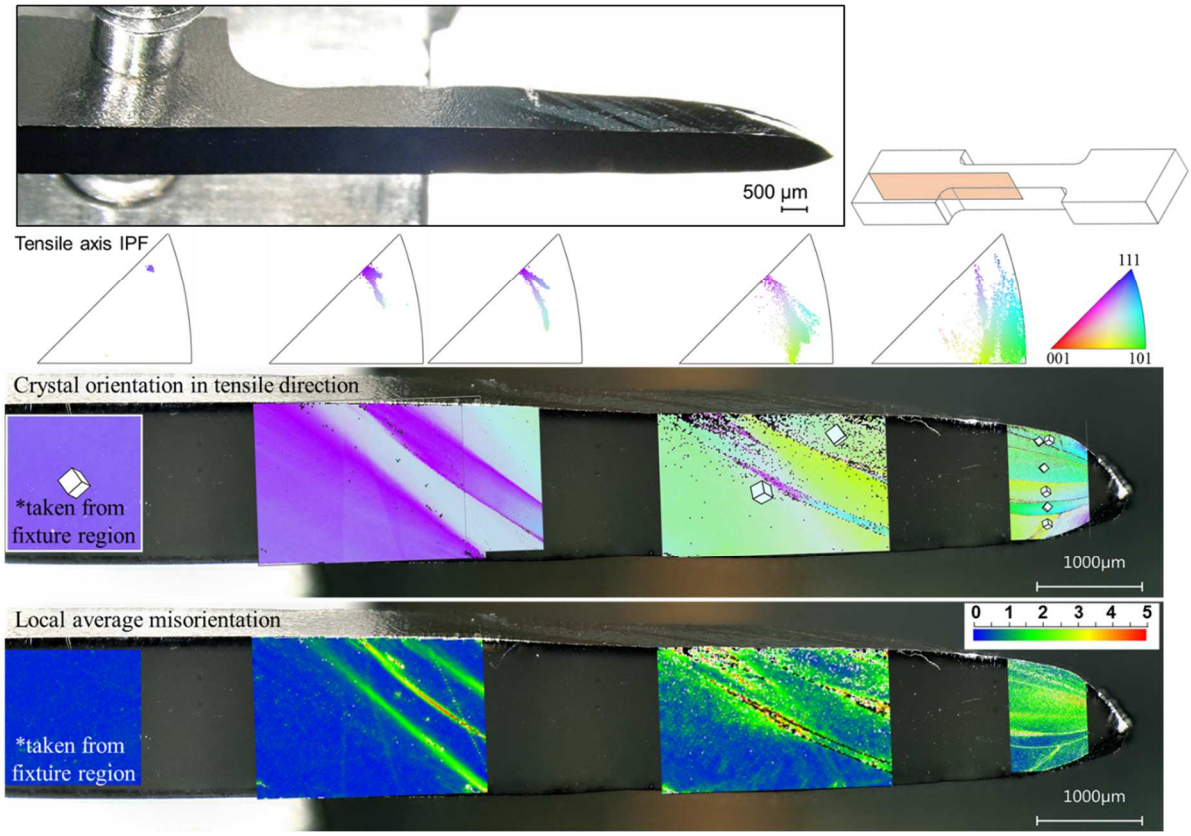

Figure 14: (Inset) optical image of specimen 5-34 showing large shear bands on the top surface of the specimen. EBSD orientation maps in the tensile direction with the corresponding orientation of 10,000 points of each map on tensile axis inverse pole figures, showing the crystal rotation from the fixture to the fracture surface, and LAM maps of the specimen deformed in tension at 10^{-2} s^{-1}.

3.8 Potential effect on Sheet Forming

The reduction in strength anisotropy at high strain rate suggests that manufacturing of SRF cavities with electro-hydraulic forming could lead to a more uniform deformation and consequently, a higher shape accuracy. Despite the lower ductility measured at higher strain rates in the uniaxial tensile tests, high-speed forming results in non-linear strain paths and multi-axial stress states during the tool–sheet interaction that can lead to strong compressive hydro-static stresses that reduce damage and delay sheet fracture [69], [70].

The difference in crystal fracture surface rotation for different crystallographic orientations clearly shows that the presence of grain boundaries will lead to a local stress concentration or strain instability. Forming using a single crystal sheet [1] would then be ideal to avoid grain boundaries and the lesser anisotropy at high strain rate indicates that the effect of the single crystal orientation may be negligible.

4 Conclusions

Mechanical properties of niobium single crystals for SRF cavity fabrication were measured using material from the same grains of an ingot for different crystallographic orientations and strain rates, from 1.28×10^{-4} s^{-1} to approximately 1000 s^{-1}. Stress anisotropy was more significant at quasi-static rates, but nearly absent at dynamic strain rates. The absence of stage I hardening for increasing

strain rates indicates the activation of multiple slip systems after yield and is believed to be a factor responsible for the reduction in stress anisotropy. However, strain anisotropy associated with the kinematics of the favored slip systems, appears to be independent of strain rate.

A transition from hardening to softening, in the majority of the plastic domain, was observed for orientations near the center of a tensile axis IPF at strain rates greater than approximately $6.4x10^{-2}$ s^{-1}. The strain rate at the transition was not identified for other orientations, but 8 specimens with different tensile orientations deformed at approximately 10 s^{-1} showed softening after yield.

Digital image correlation showed the formation of necks before failure, which could account for softening at low strains at quasi-static strain rates followed by a homogenization of strain corresponding to the hardening stage.

Fracture surfaces of tensile specimens deformed at low and high strain rates all showed chisel-edge and no crystal orientation-based trends in fracture surface edge rotation and length were observed. EBSD showed crystal rotations toward the terminal stable [101] orientation and the majority of the rotation taking place about a direction perpendicular to the tensile axis.

Shear bands leading to heterogeneous deformation were observed in two specimens deformed at $1.28x10^{-2}$ s^{-1} leading to low ductility and high hardening rates in orientations close to the top of the IPF and in the region where slip systems of the {110} and {112} families have similar low Schmid factors. Quasi-static specimens with different tensile orientations, presented in Figure 12b, and all dynamic specimens in Figure 13b showed no bands, but substantial crystal rotation from the undeformed fixture region to the fracture surface.

The reduction in stress anisotropy at high strain rates is expected to be beneficial for high-velocity forming of cavities, which should promote a more uniform strain that leads to better shape accuracy. However, a reduction in strain-to-failure was measured for increasing strain rates, along with a lack of strain hardening. Further TEM analyses on the effect of high strain rate deformation on dislocation structure are planned, as wells as the influence of the dislocations arrangement created at high strain rate on superconducting properties.

5 Acknowledgments

The authors would like to acknowledge the work of CERN's Materials, Metrology and Non-Destructive Testing (EN-MME-MM) section for granting access to their equipment for specimen preparation and scanning electron microscope (SEM) analyses. The authors would also like to thank Mr. Larry Vladic of Elite Motion LLC for lending us the high-speed camera during the high strain rate tests performed ASU. This Marie Sklodowska-Curie Action (MSCA) Innovative Training Network (ITN) receives funding from the European Union's H2020 Framework Programme under grant agreement no. 764879. T.R. Bieler, D. Kang, E. Pai Kulyadi, P. Eisenlohr, C. Kale, and K.N. Solanki acknowledge support from DOE/OHEP grant DE-SC0009962.

6 Data availability

The raw/processed data required to reproduce these findings cannot be shared at this time as the data also forms part of an ongoing study.

7 References

[1] P. Kneisel, G. R. Myneni, G. Ciovati, J. Sekutowicz, and T. Carneiro, "Preliminary Results from Single Crystal and Very Large Crystal Niobium Cavities," in *Proceedings of the 2005 Particle Accelerator Conference*, Knoxville, TN, USA, 2005, pp. 3991–3993, doi: 10.1109/PAC.2005.1591693.

[2] P. Kneisel, "Progress on large grain and single grain niobium - ingots and sheet and review of progress on large grain and single grain niobium cavities," presented at the SRF2007, Beijing, China, 2007.

[3] P. Kneisel *et al.*, "Review of ingot niobium as a material for superconducting radiofrequency accelerating cavities," *Nucl. Instrum. Methods Phys. Res. Sect. Accel. Spectrometers Detect. Assoc. Equip.*, vol. 774, pp. 133–150, Feb. 2015, doi: 10.1016/j.nima.2014.11.083.

[4] W. Singer *et al.*, "Development of large grain cavities," *Phys. Rev. Spec. Top. - Accel. Beams*, vol. 16, no. 1, Jan. 2013, doi: 10.1103/PhysRevSTAB.16.012003.

[5] J. E. Chen and K. Zhao, "The growth of SRF in China," presented at the SRF2007, Beijing, China.

[6] S. Quan *et al.*, "3.5-cell large grain niobium superconducting cavity for a dc superconducting rf photoinjector," *Phys. Rev. Spec. Top. - Accel. Beams*, vol. 13, no. 4, Apr. 2010, doi: 10.1103/PhysRevSTAB.13.042001.

[7] Z. G. Zong *et al.*, "Electro-polished cavities using china ningxia large grain niobium material," in *2007 IEEE Particle Accelerator Conference (PAC)*, Albuquerque, NM, 2007, pp. 2143–2145, doi: 10.1109/PAC.2007.4441177.

[8] J. Gao, J. P. Dai, Z. D. Guo, and I. Beijing, "First Test Result of the IHEP-01 Large Grain 9-Cell Cavity."

[9] E. Cantergiani *et al.*, "Niobium superconducting rf cavity fabrication by electrohydraulic forming," *Phys. Rev. Accel. Beams*, vol. 19, no. 11, Nov. 2016, doi: 10.1103/PhysRevAccelBeams.19.114703.

[10] R. Maddin and N. K. Chen, "Plasticity of Columbium Single Crystals," *JOM*, vol. 5, no. 9, pp. 1131–1136, Sep. 1953, doi: 10.1007/BF03397601.

[11] T. E. Mitchell, R. A. Foxall, and P. B. Hirsch, "Work-hardening in niobium single crystals," *Philos. Mag.*, vol. 8, no. 95, pp. 1895–1920, Nov. 1963, doi: 10.1080/14786436308209081.

[12] R. A. Foxall, M. S. Duesbery, and P. B. Hirsch, "The deformation of niobium single crystals," *Can. J. Phys.*, vol. 45, no. 2, pp. 607–629, Feb. 1967, doi: 10.1139/p67-052.

[13] M. S. Duesbery, R. A. Foxall, and P. B. Hirsch, "The plasticity of pure niobium single crystals," *J. Phys. Colloq.*, vol. 27, no. C3, pp. C3-193-C3-204, Jul. 1966, doi: 10.1051/jphyscol:1966325.

[14] M. S. Duesbery and R. A. Foxall, "A detailed study of the deformation of high purity niobium single crystals," *Philos. Mag.*, vol. 20, no. 166, pp. 719–751, Oct. 1969, doi: 10.1080/14786436908228040.

[15] D. K. Bowen, J. W. Christian, and G. Taylor, "Deformation properties of niobium single crystals," *Can. J. Phys.*, vol. 45, no. 2, pp. 903–938, Feb. 1967, doi: 10.1139/p67-069.

[16] P. J. Sherwood, F. Guiu, H. C. Kim, and P. L. Pratt, "Plastic Anisotropy of Tantalum, Niobium, and Molybdenum," *Can. J. Phys.*, vol. 45, no. 2, pp. 1075–1089, Feb. 1967, doi: 10.1139/p67-079.

[17] A. Ermakov *et al.*, "Physical properties and structure of large grain/single crystal niobium for superconducting RF cavities," *J. Phys. Conf. Ser.*, vol. 97, p. 012014, Feb. 2008, doi: 10.1088/1742-6596/97/1/012014.
[18] D. C. Baars, T. R. Bieler, and C. Compton, "Microstructure Studies of Niobium," presented at the SRF2009, Berlin, Germany, 2009.
[19] D. Baars, "Investigation of active slip systems in high purity single crystal niobium," Ph. D. Thesis, Michigan State University, East Lansing, MI, 2013.
[20] D. Kang, D. C. Baars, and T. R. Bieler, "Study of Slip and Deformation in High Purity Single Crystal Nb for Accelerator Cavities," presented at the SRF2015, 2015.
[21] G. R. Myneni, "Physical and Mechanical Properties of Niobium for SRF Science and Technology," in *AIP Conference Proceedings*, Araxa, Brazil, 2007, vol. 927, pp. 41–47, doi: 10.1063/1.2770677.
[22] T. Gnäupel-Herold, G. R. Myneni, and R. E. Ricker, "Investigations of Residual Stresses and Mechanical Properties of Single Crystal Niobium for SRF Cavities," in *AIP Conference Proceedings*, Araxa (Brazil), 2007, vol. 927, pp. 48–59, doi: 10.1063/1.2770678.
[23] R. E. Ricker, D. J. Pitchure, and G. R. Myneni, "Mechanical properties as an indicator of interstitials in niobium for superconducting accelerator cavities," presented at the Science and Technology of Ingot Niobium for Superconducting Radio Frequency Applications, Virginia, USA, 2015, doi: 10.1063/1.4935319.
[24] J. Nagakawa and M. Meshii, "The deformation of niobium single crystals at temperatures between 77 and 4.2 K," *Philos. Mag. A*, vol. 44, no. 5, pp. 1165–1191, Nov. 1981, doi: 10.1080/01418618108235801.
[25] T. S. Byun, S.-H. Kim, and J. Mammosser, "Low-temperature mechanical properties of superconducting radio frequency cavity materials," *J. Nucl. Mater.*, vol. 392, no. 3, pp. 420–426, Aug. 2009, doi: 10.1016/j.jnucmat.2009.03.058.
[26] W. F. Hosford, *The mechanics of crystals and textured polycrystals*. New York: Oxford University Press, 1993.
[27] I. M. Robertson *et al.*, "Hydrogen Embrittlement Understood," *Metall. Mater. Trans. B*, vol. 46, no. 3, pp. 1085–1103, Jun. 2015, doi: 10.1007/s11663-015-0325-y.
[28] M. Nagumo, *Fundamentals of Hydrogen Embrittlement*. Singapore: Springer Singapore, 2016.
[29] K. V. Ravi and R. Gibala, "The strength of niobium-oxygen solid solutions," *Acta Metall.*, vol. 18, no. 6, pp. 623–634, Jun. 1970, doi: 10.1016/0001-6160(70)90091-X.
[30] K. V. Ravi and R. Gibala, "Low temperature strengthening in niobium-hydrogen single crystals," *Metall. Trans.*, vol. 2, no. 4, pp. 1219–1225, Apr. 1971, doi: 10.1007/BF02664255.
[31] W. Singer, "SRF Cavity Fabrication and Materials," *CERN Yellow Rep. CERN-2014-005*, pp. 171–207, 2015, doi: 10.5170/CERN-2014-005.171.
[32] D. Kang, D. C. Baars, T. R. Bieler, and C. C. Compton, "Characterization of Large Grain Nb Ingot Microstructure Using EBSP Mapping and Laue Camera Methods," Virginia, (USA), 2011, pp. 90–99, doi: 10.1063/1.3579228.
[33] H.-J. Bunge, *Texture Analysis in Materials Science: Mathematical Methods.* Cambridge: Elsevier Science, 1982.
[34] S. A. Turnage, "Anomalous Dynamic Behavior of Stable Nanograined Materials," PhD Thesis, Arizona State University, Tempe, AZ, 2017.
[35] S. A. Turnage *et al.*, "Influence of variable processing conditions on the quasi-static and dynamic behaviors of resistance spot welded aluminum 6061-T6 sheets," *Mater. Sci. Eng. A*, vol. 724, pp. 509–517, May 2018, doi: 10.1016/j.msea.2018.03.120.
[36] W. R. Whittington *et al.*, "Capturing the effect of temperature, strain rate, and stress state on the plasticity and fracture of rolled homogeneous armor (RHA) steel," *Mater. Sci. Eng. A*, vol. 594, pp. 82–88, Jan. 2014, doi: 10.1016/j.msea.2013.11.018.
[37] ASTM International, "ASTM E8 / E8M-16ae1, Standard Test Methods for Tension Testing of Metallic Materials." 2016, [Online]. Available: astm.org.

[38] S. Yoo, D. Schueler, M. Brodbeck, N. Toso, G. Catalanotti, and H. Voggenreiter, “An Improved Load Introduction Technique for Dynamic Material Characterisation at Intermediate Strain Rate,” *Proceedings*, vol. 2, no. 8, p. 381, May 2018, doi: 10.3390/ICEM18-05203.
[39] C. Kale *et al.*, “On the roles of stress-triaxiality and strain-rate on the deformation behavior of AZ31 magnesium alloys,” *Mater. Res. Lett.*, vol. 6, no. 2, pp. 152–158, Feb. 2018, doi: 10.1080/21663831.2017.1417923.
[40] C. Kale, S. Turnage, D. Z. Avery, H. El Kadiri, J. B. Jordon, and K. N. Solanki, “Towards dynamic tension-compression asymmetry and relative deformation mechanisms in magnesium,” *Materialia*, vol. 9, p. 100543, Mar. 2020, doi: 10.1016/j.mtla.2019.100543.
[41] D. J. Barton, C. Kale, B. C. Hornbuckle, K. A. Darling, K. N. Solanki, and G. B. Thompson, “Microstructure and dynamic strain aging behavior in oxide dispersion strengthened 91Fe-8Ni-1Zr (at%) alloy,” *Mater. Sci. Eng. A*, vol. 725, pp. 503–509, May 2018, doi: 10.1016/j.msea.2018.04.016.
[42] S. A. Turnage *et al.*, “Anomalous mechanical behavior of nanocrystalline binary alloys under extreme conditions,” *Nat. Commun.*, vol. 9, no. 1, p. 2699, Jul. 2018, doi: 10.1038/s41467-018-05027-5.
[43] W. W. Chen and B. Song, *Split Hopkinson (Kolsky) bar: design, testing and applications*. New York, NY: Springer, 2011.
[44] G. Nolze and R. Hielscher, “Orientations – perfectly colored,” *J. Appl. Crystallogr.*, vol. 49, no. 5, pp. 1786–1802, Oct. 2016, doi: 10.1107/S1600576716012942.
[45] T. E. Mitchell and W. A. Spitzig, “Three-stage hardening in tantalum single crystals,” *Acta Metall.*, vol. 13, no. 11, pp. 1169–1179, Nov. 1965, doi: 10.1016/0001-6160(65)90054-4.
[46] J. W. Hutchinson and K. W. Neale, “Influence of strain-rate sensitivity on necking under uniaxial tension,” *Acta Metall.*, vol. 25, no. 8, pp. 839–846, Aug. 1977, doi: 10.1016/0001-6160(77)90168-7.
[47] A. K. Ghosh, “The Influence of Strain Hardening and Strain-Rate Sensitivity on Sheet Metal Forming,” *J. Eng. Mater. Technol.*, vol. 99, no. 3, pp. 264–274, Jul. 1977, doi: 10.1115/1.3443530.
[48] Y. Rotbaum and D. Rittel, “Is There An Optimal Gauge Length for Dynamic Tensile Specimens?,” *Exp. Mech.*, vol. 54, no. 7, pp. 1205–1214, Sep. 2014, doi: 10.1007/s11340-014-9889-8.
[49] P. Verleysen, J. Degrieck, T. Verstraete, and J. Van Slycken, “Influence of Specimen Geometry on Split Hopkinson Tensile Bar Tests on Sheet Materials,” *Exp. Mech.*, vol. 48, no. 5, pp. 587–598, Oct. 2008, doi: 10.1007/s11340-008-9149-x.
[50] L. Peroni and M. Scapin, “Experimental analysis and modelling of the strain-rate sensitivity of sheet niobium,” *EPJ Web Conf.*, vol. 183, 2018, doi: 10.1051/epjconf/201818301014.
[51] K. G. Hoge and A. K. Mukherjee, “The temperature and strain rate dependence of the flow stress of tantalum,” *J. Mater. Sci.*, vol. 12, no. 8, pp. 1666–1672, Aug. 1977, doi: 10.1007/BF00542818.
[52] F. J. Zerilli and R. W. Armstrong, “Description of tantalum deformation behavior by dislocation mechanics based constitutive relations,” *J. Appl. Phys.*, vol. 68, no. 4, pp. 1580–1591, Aug. 1990, doi: 10.1063/1.346636.
[53] G. Z. Voyiadjis and F. H. Abed, “Effect of dislocation density evolution on the thermomechanical response of metals with different crystal structures at low and high strain rates and temperatures,” p. 45, 2005.
[54] A. Rusinek, R. Zaera, J. Klepaczko, and R. Cheriguene, “Analysis of inertia and scale effects on dynamic neck formation during tension of sheet steel,” *Acta Mater.*, p. S1359645405004775, Oct. 2005, doi: 10.1016/j.actamat.2005.08.019.
[55] G. Regazzoni and F. Montheillet, “High Strain Rate Ductility in Uniaxial Tension: A Review,” *J. Phys. Colloq.*, vol. 46, no. C5, pp. C5-435-C5-444, Aug. 1985, doi: 10.1051/jphyscol:1985554.

[56] M. A. Bhatia, S. Groh, and K. N. Solanki, “Atomic-scale investigation of point defects and hydrogen-solute atmospheres on the edge dislocation mobility in alpha iron,” *J. Appl. Phys.*, vol. 116, no. 6, p. 064302, Aug. 2014, doi: 10.1063/1.4892630.
[57] G. T. (Rusty) Gray, “High-Strain-Rate Testing of Materials: The Split-Hopkinson Pressure Bar,” in *Characterization of Materials*, E. N. Kaufmann, Ed. Hoboken, NJ, USA: John Wiley & Sons, Inc., 2012.
[58] V. S. Balanethiram and G. S. Daehn, “Hyperplasticity: Increased forming limits at high workpiece velocity,” *Scr. Metall. Mater.*, vol. 30, no. 4, pp. 515–520, Feb. 1994, doi: 10.1016/0956-716X(94)90613-0.
[59] G. R. Myneni, “Physical and Mechanical Properties of Single and Large Crystal High-RRR niobium,” presented at the SRF2005, Ithaca, NY, USA, 2005.
[60] H. Conrad, “Thermally activated deformation of metals,” *JOM*, vol. 16, no. 7, pp. 582–588, Jul. 1964, doi: 10.1007/BF03378292.
[61] T. E. Mitchell, “Dislocations and plasticity in single crystals of face-centered cubic metals and alloys,” *Prog. Appl. Mater. Res.*, vol. 6, pp. 119–237, 1964.
[62] T. Suzuki, S. Takeuchi, and H. Yoshinaga, *Dislocation Dynamics and Plasticity*. Berlin, Heidelberg: Springer Berlin Heidelberg, 1991.
[63] T. Suzuki, H. Koizumi, and H. O. K. Kirchner, “Plastic flow stress of b.c.c. transition metals and the Peierls potential,” *Acta Metall. Mater.*, vol. 43, no. 6, pp. 2177–2187, Jun. 1995, doi: 10.1016/0956-7151(94)00451-X.
[64] A. F. Liu, *Mechanics and mechanisms of fracture: an introduction*. Materials Park, Ohio: ASM International, 2005.
[65] S. Simoto, W. F. Hosford, and W. A. Backofen, “Ductile fracture in copper single crystals,” *Philos. Mag.*, vol. 12, no. 116, pp. 319–333, Aug. 1965, doi: 10.1080/14786436508218874.
[66] N. Jia, P. Eisenlohr, F. Roters, D. Raabe, and X. Zhao, “Orientation dependence of shear banding in face-centered-cubic single crystals,” *Acta Mater.*, vol. 60, no. 8, pp. 3415–3434, May 2012, doi: 10.1016/j.actamat.2012.03.005.
[67] D. Dorner, Y. Adachi, and K. Tsuzaki, “Periodic crystal lattice rotation in microband groups in a bcc metal,” *Scr. Mater.*, vol. 57, no. 8, pp. 775–778, Oct. 2007, doi: 10.1016/j.scriptamat.2007.06.048.
[68] Z. Zhao, T. R. Bieler, and D. Kang, “An Investigation of Correlations Between Mechanical and Microstructural Properties of High Purity Polycrystalline Niobium,” Whistler, Canada, Sep. 2015, vol. C08, pp. 219–222.
[69] J. M. Imbert, S. L. Winkler, M. J. Worswick, D. A. Oliveira, and S. Golovashchenko, “The Effect of Tool–Sheet Interaction on Damage Evolution in Electromagnetic Forming of Aluminum Alloy Sheet,” *J. Eng. Mater. Technol.*, vol. 127, no. 1, pp. 145–153, Jan. 2005, doi: 10.1115/1.1839212.
[70] S. F. Golovashchenko, A. J. Gillard, and A. V. Mamutov, “Formability of dual phase steels in electrohydraulic forming,” *J. Mater. Process. Technol.*, vol. 213, no. 7, pp. 1191–1212, Jul. 2013, doi: 10.1016/j.jmatprotec.2013.01.026.